Egypt. J. Chem. **Vol. 68,** No. 10 pp. 479 - 491 (2025)

Egyptian Journal of Chemistry

http://ejchem.journals.ekb.eg/

Fabrication of p-type Porous Silicon Powder via Facile and Economic Preparation Method

Raghda Nomair[*1], Marwa Nabil[2], Mohamed Elnouby[2], E. M. El-Maghraby[1]

[1]*Department of Physics, Faculty of Science, Damanhour University, Damanhur 22511, Egypt*
[2]*Advanced Technology and New Materials Research Institute, City for Scientific, Research and Technology Applications (SRTA City), New Borg El-Arab City 21934, Egypt*

Abstract

This study demonstrates the use of powder technology manufacturing as an innovative, affordable, easy, and secure technique for the creation of p-type nano-porous silicon powder (p-NPS powder). NPS powder doped with B, Ni, and Cd using a combination of alkali chemical etching and the hydrothermal technique. Structural analysis via X-Ray Diffraction (XRD) confirmed NPS crystal has a cubic structure, and there was some distortion in the structure after doping, while Fourier Transform Infrared Spectroscopy (FTIR) and Energy-Dispersive X-ray (EDX) analysis verified elemental incorporation. Scanning Electron Microscopy (SEM) images revealed morphological changes due to doping, and a 3D model of the crystal lattice, generated using VESTA software, illustrated the structural modifications induced by dopant atoms. Optical absorption studies using UV-Vis spectroscopy demonstrated a decrease in band gap for NPS-B (2.0 eV), NPS-Ni (1.7 eV), and NPS-Cd (1.6 eV) compared to un-doped NPS (2.4 eV). The reduction in band gap is attributed to impurity-induced states, quantum confinement reduction, and defect formation, which modify the electronic structure of the material. These findings highlight the potential of doped NPS for applications in optoelectronic devices and sensors.

Keywords: doping, p-type porous silicon, hydrothermal technique, X-ray diffraction, 3D crystal model

1. Introduction

Over the past few years, significant studies on research have been attached to materials with nanostructures because of their wide-ranging uses in several scientific and technological domains. Consequently, the commercial and effective production of these substances is remarkable, particularly if they are intended for widespread use [1]. NPS is one of many nanomaterials that have numerous promising applications in many fields [2], such as optical devices [3], biomedical devices [4], transistors [5], improving catalysts [6], gas sensors [7], environmental applications [8], and electrochemical sensors [9]. In our previous study [10], we fabricated NPS powder using a hybrid of the ultra-sonication technique and the alkali chemical etching process started by commercial polycrystalline silicon powder [11].

Previous researches showed the doping process of Si wafers using different elements and several techniques. Boron and phosphorus are the most famous elements that are used as dopants for the formation of p-type and n-type bulk silicon to improve its electronic and optical properties [12]. Bulk impurities of nickel and copper in the highly doped p-type silicon wafers to assess the relationship between them, rate of recovery, and sensitivity [13]. Using instrumental neutron activation studies, nickel in intrinsic, moderately, and severely doped n-type and p-type silicon was determined [14]. Both n- and p-type silicon were doped with nickel to disclose three electrical levels of substitution nickel in silicon [15]. Cadmium-doped silicon was found to be an appropriate dopant for work on defect-engineering to increase silicon's radiation toughness in preparation for high-energy experiments in physics [16]. But till now, no study has addressed the doping process for NPS powder.

In the case of porous silicon (PS), boron element-doped PS wafers were effectively created and ready through the air-oxidation demagnetization of Mg_2Si from p-type Si wafers [16]. On the other hand, phosphorus element-doped PS wafers were prepared via magnesio-thermic reduction of cross-linked nanosized P-SiO_2 precursors. The obtained PS wafers with a proper surface area are highly crystalline and conductive [17]. Nickel-doped p-type silicon wafers via several methods: wafer digestion, poly-silicon ultra-trace profiling, and low-temperature out-diffusion [13]. Two techniques are used to dope n- and p-type silicon with nickel. First, during growth, the initial set of n- and p-type silicon wafers was purposefully doped with nickel. Second, set n- and p-type silicon was used, in which vacancies were created by a high-temperature annealing and stabilized by nitrogen gas [18]. Cadmium-doped silicon via diffusion of cadmium into silicon occurs through interstitial and vacancy mechanisms [16]. The high surface area and sensitivity of p-type PS to chemicals

---

*Corresponding author e-mail: raghda.mhmd91@yahoo.com.; (Raghda Nomair).
Received date 01 February, 2025; Revised date 24 February, 2025; Accepted date 05 March 2025
DOI: 10.21608/EJCHEM.2025.356086.11243

make it suitable for gas sensors [19]. Changes in electrical conductivity or optical properties can be exploited for sensing applications [20].

Recent studies have demonstrated the hydrothermal technique's capacity to dope and synthesize a wide variety of materials [21, 22]. The hydrothermal technique is described as any homogeneous nanoparticle reaction materials that are insoluble under normal circumstances can be dissolved and recrystallized in the presence of aqueous solutions at high pressure and temperature [23]. This process is used to control nanostructures by using variable parameters that have an obvious effect on doping and structure [24].

In this work, starting with synthesized NPS powder, that straightforward synthetic route for the powder manufacture of p-NPS of various structures is employed, combining the alkali chemical etching procedure with the hydrothermal technique. As a new, inexpensive, safe method for preparing doped NPS powder. It is a cutting-edge process for making p-NPS powder in large numbers with excellent yield efficiency.

2. Materials and Methods

2.1. NPS Powder Manufacturing

The fusion of two methods (alkali chemical etching and ultra-sonication) for the manufacturing of NPS powder was carried out, beginning with Si-powder that was sold commercially. (Silicium, Pulver-99%, Burlington, VT, USA), as demonstrated by our earlier research [11]. A sufficient quantity of Si powder was distributed in potassium hydroxide [KOH M= 56.11 g/mol] supplied by SIGMA-ALDRICH, and NPA n-propanol [C_3H_8O M= 60.10 g/mol] was supplied by POLSKIE ODCZYNNIKI CHEMICZNE S.A. scattered throughout ultrapure water [18 MΩ deionized water]. After filtering and washing, the product powders were left to dry overnight.

2.2. Preparation of doped NPS Powder (using Boric acid, Nickel Chloride, and Cadmium Chloride)

Due to the use of the hydrothermal technique, the etching mixture solution, which contains NPS powder (2.0 g) distributed in KOH, NPA, and boric acid, 99.5% [H_3BO_3, M= 61.833 g/mol, which was supplied by SPECTRUM] (0.5 gm), Nickel (II) Chloride Hydrate, 99.95% [$NiCl_2{\cdot}6H_2O$ M= 129.60 g/mol, which was supplied by ALDRICH] (0.5 gm), and Cadmium Chloride Hemi-Penta-hydrate (as $CdCl_2$ 81%) [$CdCl_2.2.5H_2O$ M= 228.34 g/mol, which was supplied by Rashmi Diagnostics Bangalore, India] (0.5 gm) were mixed separately and heated to 200°C (ramp rate: 5°C min^{-1}) for 3 hours in a muffle furnace. Once it has naturally cooled to ambient temperature, the powder product is filtrated and washed using ultrapure water [18 MΩ deionized water], then dried for one hour at 60°C.

2.3. Characterizations

Characteristics of the powder structure are obtained via XRD (X-ray diffractometer, using Cu-Kα radiation = 1.5405 Å at a scanning rate of 4 min^{-1}, 7000 Schimadzu diffractometer). The crystallite size and lattice characteristics of a subset of samples were ascertained by Rietveld refinement investigations utilizing the EXPO software. The powders were explored elementary by JEOL 5300 scanning electron microscope embedded with EDX microanalysis. The process's chemical bond creation was ascertained by FTIR (Fourier Transform Infrared Spectrophotometer, Shimadzu FTIR-8400s, Japan). The study of powder morphology makes use of SEM (scanning electron microscopy, JEOL (JSM –IT200), magnification (1000–50000)). The energy band gap value is calculated via the UV-Visible Spectrophotometer Double Auto Cell (Labomend, INC, Los Angeles, CA, USA).

3. Results and discussion

Powder Characterization

Using several physicochemical techniques, the structure and characteristics of the chemically generated material in powder form were examined.

3.1. X-ray Diffraction (XRD) analysis

The X-ray diffraction (XRD) patterns of each produced sample are displayed in Fig. 1. A JCPDS standard database was used to compare the derived XRD patterns (JCPDS Cards No. 01-079-0613 and 00-027-1402), This validates the single phase Si in each of the three scenarios. Figures (1-3) all of them show the full width at half maximum (FWHM) of the peaks around 28.51°, 47.43°, 56.28°, 69.33°and 76.60° which correspond to (111), (220), (211), (400), and (331), respectively. All of the Si powder samples were found to have face-centered cubic (fcc) crystal structures with space group Fd3m. The computed lattice parameters were a = b = c = 5.433 Å for the received silicon. There was a little drop in the lattice parameter in the nickel and cadmium doped samples (5.425, and 5.429 Å), respectively, and there was little increase shift in main peaks 28.23°, 47.193°, 56.023°, 68.989°, 76.261° as shown in the previous study [11], this demonstrates that dopant atoms have an impact on some silicon atoms.

In addition, some diffraction peaks of Boron (B) that have intensity values lower than Si diffraction peaks are at 2θ = 28.57°, 47.46°, 56.31°, 69.25°, and 76.60° which correspond to (220), (331), (412), (621), and (710), respectively (JCPDS cards No. 03-065-2859 and 01-077-3524), as shown in Fig. 1. The appearance of the boron planes is due to the reaction between the doping NPS and B atoms. The peaks' comparatively high intensities show how highly crystallized the powder is comparing to XRD pattern of NPS referred to in the previous study [11].

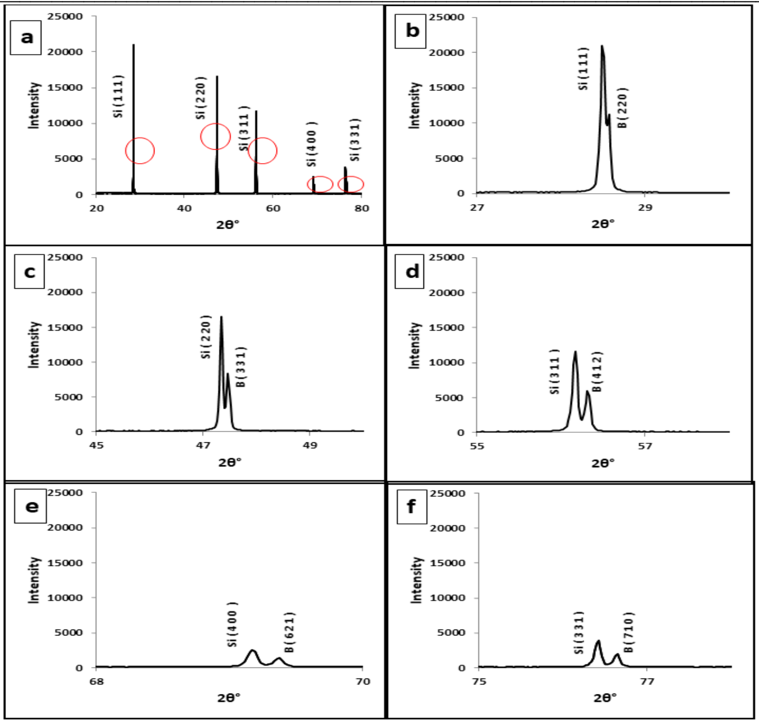

Fig.1 a) XRD pattern of 2 gm of NPS powder at hydrothermal time of 3 hr at 200 °C doping with 0.5 gm of H_3BO_3, and b to f) magnification of certain regions.

Fig. 2(a) shows the XRD pattern of sample NPS doped with nickel chloride that validates the main peaks of the single phase Si, and Fig. 2(b) is the magnification of a certain region that confirms the nickel (Ni) phase at 2θ = and 76.60°, which corresponds to (2 2 0) (JCPDS card No. COD 9009862**)**. The appearance of the nickel plane is due to the doping process of NPS by Ni atoms. So, the increase in the Si peak intensities values that appears is due to the doping process using Ni ions.

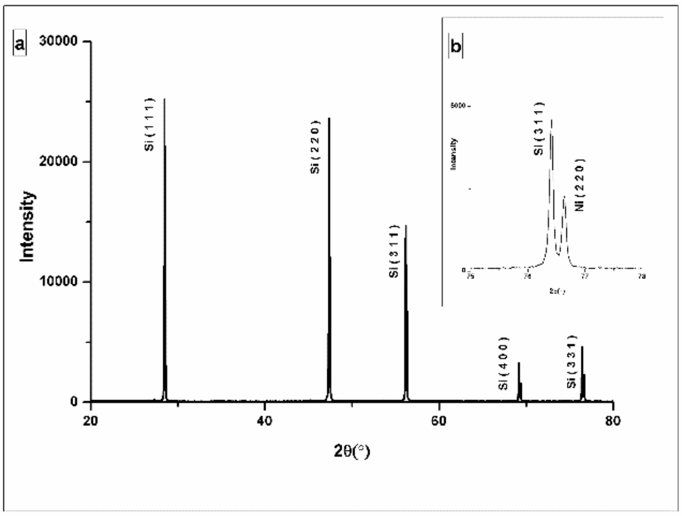

Fig.2 XRD pattern of; a) pure NPS (2 gm) powder using hydrothermal technique at 3 hr and 200°C using 0.5 gm of $NiCl_2{\cdot}6H_2O$, and b) magnification of certain region.

Fig. 3 shows an XRD pattern of sample NPS doped with cadmium chloride that validates the main peaks in the single-phase Si. Fig. 3(b-c) show the magnification of certain regions, which indicates the presence of cadmium (Cd) diffraction peaks that appear at 2θ = 47.47° and 76.60°, which correspond to planes (102) and (201), respectively (JCPDS cards No. 03-065-1183 and 00-001-1178). The appearance of the cadmium planes is due to the doping of NPS by Cd atoms. Noticeably, the sharp peak of the Si plane indicates an improvement in the crystalline quality of the Si powder. In addition, the appearing of the sharp peaks of Cd had the highest intensity peaks in all of the used dopants, as shown in Fig. (1-2).

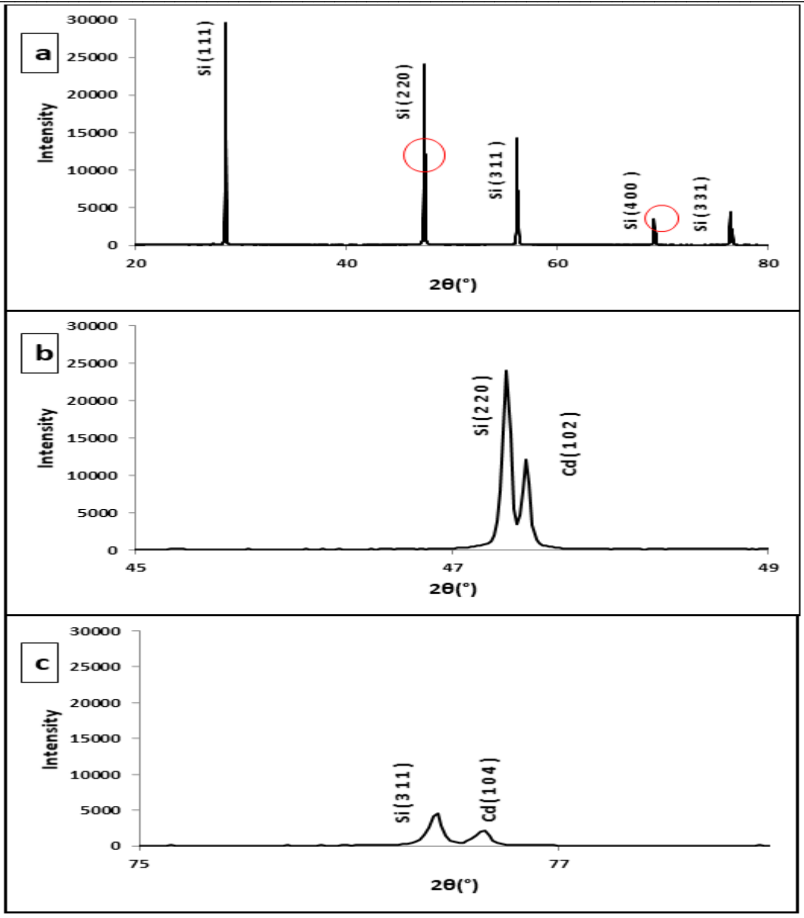

Fig.3 XRD pattern of 2 gm of NPS powder at hydrothermal time of 3 hr at 200 °C doping with 0.5 gm of $CdCl_2 \cdot 2,5H_2O$, and b-c) magnification of certain regions.

It was perceived that the dopants affect the intensity of the diffraction peaks. The pore size of the NPS is in the range of 0.28-1.40 µm, as mentioned in our previous research [11]. So, since the atomic radius of B, Ni, and Cd are 85, 135, and 155 pm, respectively, it is expected that they will enter the pores of the NPS, and thus they will merge, and the process has already taken place. That includes the impact of the dopant materials on NPS properties. Accordingly, the intensity increased, as shown in Fig. 4. In addition, the NPS material was affected by dopant materials. Thus, the shift in electron density is what causes the dopant intensity to increase, indicating a good crystallinity quality. Overall, when dopant materials are added in greater amount, the diffraction peaks intensify. Also, we noticed that the surface energy increased through the (111), (220), (311), (400), and (331) planes by adding B, Ni, and Cd to NPS. However, the orientation not only depends on the natural characteristics of materials but also on the doping conditions, such as hydrothermal time and temperature.

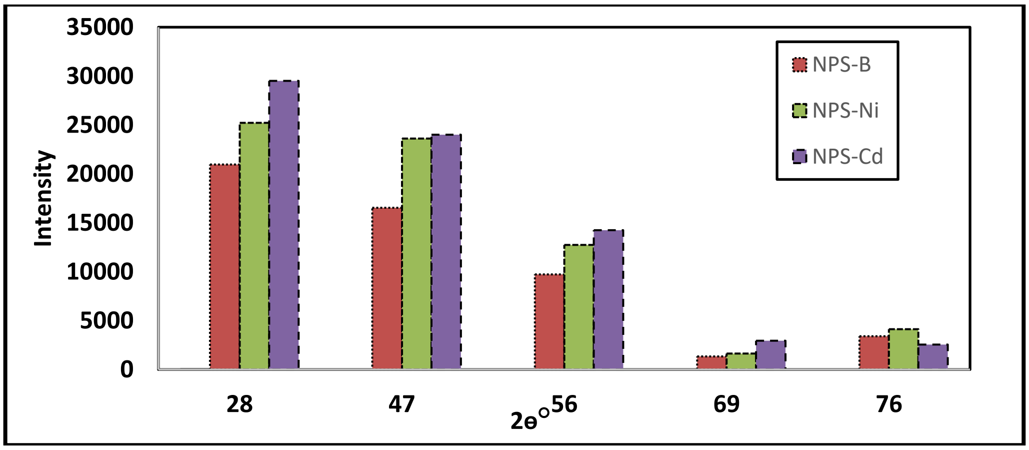

Fig.4 Effect of doping on XRD intensity peaks.

The NPS structure was characterized by using the Rietveld refinement method with EXPO software [25]. Rietveld texture analysis is a method that utilizes X-ray diffraction data to analyze the structure of the crystals of materials. It addresses the challenge of accurately determining the structure by separating overlapping peaks in the diffraction pattern, which can be imprecise due to their broad and complete overlap. This analysis solves the problem of overlapping peaks, offering a workable way to gain a comprehensive understanding of the material's structure [26]. However, the Rietveld refinement method has drawbacks such as noise, lack of clarity in XRD data, and extensively overlapped peaks. Despite these limitations, the calculated patterns using adjusted measured data provide important structural parameters and a diffraction profile [27]. Background, lattice parameters, scale factor, profile half width, crystallite size, and spatial coordinates were among the refined parameters that were included [28]. The structural properties of the NPS powders may be calculated with extreme accuracy thanks to the chosen parameters.

Rietveld refinements were used in this work to focus on the determination of the lattice parameter. R-expected (R_e), R-pattern (R_p), R-Bragg factor (R_B), R-weighted pattern (R_{wp}), Chi-*square* (χ^2), lattice parameters (a, b, c), and crystallite size (L (nm)) are presented in Table 1. The calculated R index values listed in Table.1 that indicates a good refinement result. The Chi ^{2} based on the ratio $[R_{wp}/R_e]^2$, contains lower values for each sample that indicating better model fit.

Furthermore, the lattice parameter (a) was found. Thus, variations in the lattice parameter concerning the dopant material were noted. Table 1 displays the values of the lattice parameters for the NPS, NPS-B, NPS-Ni, and NPS-Cd samples, which are 5.443 Å, 5.444 Å, 5.425 Å, and 5.429 Å, respectively. The crystal cell decreased in NPS-Ni and NPS-Cd can be attributed to the doping of nickel and cadmium in NPS, with respect to the values of ionic radius for Ni and Cd being 0.69 Å and 0.97 Å [30], respectively. Due to the ionic radius of Ni and Cd that is larger than the ionic radius for Si 0.4 Å [30], which leads to modifications in the silicon lattice. However, the smaller size of Ni relative to Cd causes more significant distortions as the Ni ions attempt to substitute Si in the lattice or occupy interstitial positions. This is evident in the observed lattice parameter reduction for NPS-Ni (5.425 Å) compared to NPS-Cd (5.429 Å). The contraction suggests a higher degree of strain in the Ni-doped sample.

There is a direct proportionality between crystallite size and amounts of dopant material. So, it causes the crystalline lattice to expand. Finding out how much the doping process has caused the crystallite size to expand and contract depends on the ionic radius [31]. Also, Ni exhibits stronger covalent bonding tendencies with Si, unlike Cd. This results in increased localized strain and defect formation in NPS-Ni. The formation of shear bands, as indicated in the analysis, further corroborates the higher degree of disorder in Ni-doped samples throughout the hydrothermal process.

Table 1 shows the experimental data from EXPO software and crystallite size, which is calculated using the Debye Scherer equation [32]. Its values are registered as follows: 79.412, 79.414, and 79.412 nm, respectively. The NPS-Ni has less unit cell volume than the NPS, which can be associated with the dissolution of some Ni into the NPS. We noticed that the main structure is cubic, and there appears to be some distortion in the structure as a result of doping, as is clear in the ratio of intensity between peaks, as shown in Table 1. Furthermore, Table 1 shows that all dopant materials pass into NPS powder, and the best dopant material is NPS-Ni.

Table 1: Refinement results of NPS and doped NPS using different dopants.

Samples	NPS	NPS-B	NPS-Ni	NPS-Cd
a (Å)	5.443	5.444	5.425	5.429
b (Å)	5.443	5.443	5.413	5.426
c (Å)	5.443	5.443	5.429	5.413
V (Å^3)	161.41	161.31	159.79	161.32
R_B (%)	17.50	23.21	25.20	25.07
R_p (%)	16.84	21.99	20.25	29.02
R_{wp}(%)	22.00	31.54	27.22	38.87
Re (%)	17.32	16.85	17.02	17.05
χ^2	1.27	1.87	1.59	2.27
L (nm)	25.875	79.412	79.414	79.412

Fig. 5 presents a comparison of the fitted data produced with the sample's observed pattern using EXPO software. The red line represents the fitted formula obtained through the least squares method, whereas the prepared sample's and reference's peak positions are below the diffraction pattern. Overall, Fig. 5(a-d) shows the experimental and calculated X-ray diffraction patterns of the doped materials and the difference between the calculated and observed diffraction patterns. The doped martial has sharper peaks than NPS, which is at least for the larger crystallite size; it also showed a little decrease in a-lattice parameter due to doping and demonstrates a satisfactory fit between the observed pattern and the fitting profile.

The final values of the discrepancy factors for NPS-B were as follows: Rp = 21.99% and R_B = 23.21% and the discrepancy factors for NPS-Ni were as follows: Rp = 20.25% and R_B = 25.20%. Before the positions of B and Ni atoms were introduced into the structural model of NPS, the discrepancy factors had considerably lower values: Rp = 16.84% and R_B = 17.50%. So, the NPS-B and NPS-Ni factors are lower than NPS-Cd, which means doping with B and Ni is the best than Cd, as a lower R_B is better to fit.

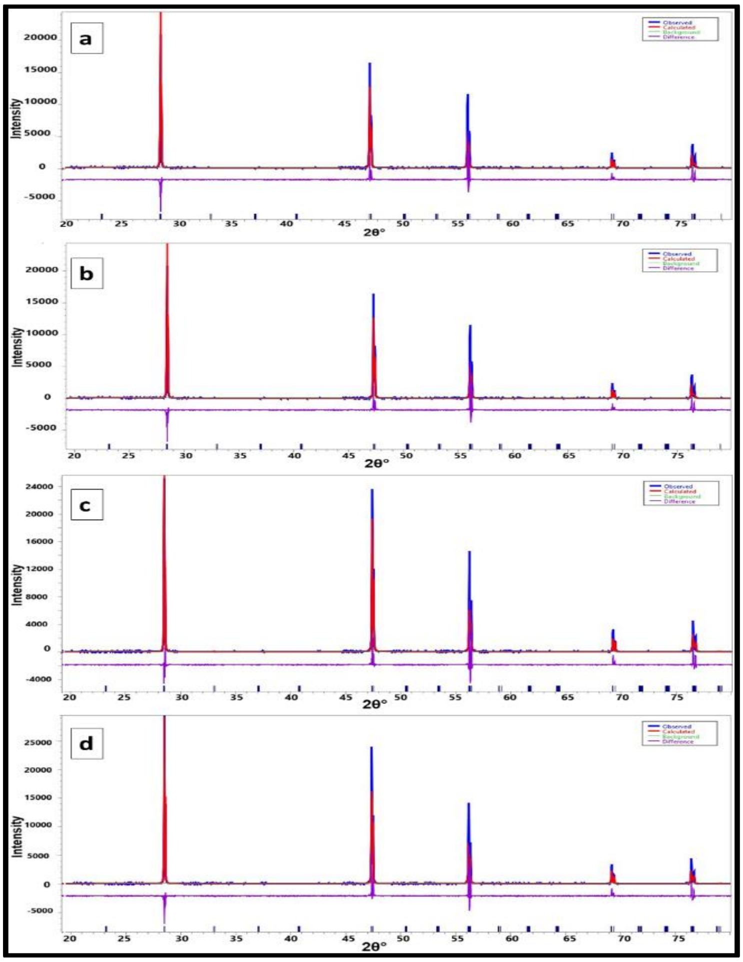

Fig.5 a) XRD patterns and Rietveld refinement of 2 gm NPS powder at hydrothermal time of 3 hr at 200 C^o, b) (NPS-B) doping with 0.5 gm of H_3BO_3; c) (NPS-Ni) doping with 0.5 gm $NiCl_2·6H_2O$; and d) (NPS-Cd) doping with 0.5 gm $CdCl_2·2,5H_2O$.

The 3D model lattice crystal, which was predicted using VESTA software [33], is displayed in Fig. 6 and depicts a cubic structure containing molecules as well as the placement of atoms in the NPS's structural channels following doping. Fig. 6(b). One direction (X) in NPS-B changed, while the other two directions (Y and Z) remained the same. However, as Fig. 6(c) illustrates, in the instance of NPS-Ni, there was a shift in one direction (Y), and the other two directions (X and Z) were also altered. In contrast, Fig. 6(d) displays NPS-Cd with adjustments in one direction (Z) but no changes in the other two directions (X and Y). Thus, it demonstrates how the doping process in NPS varies with different dopant materials.

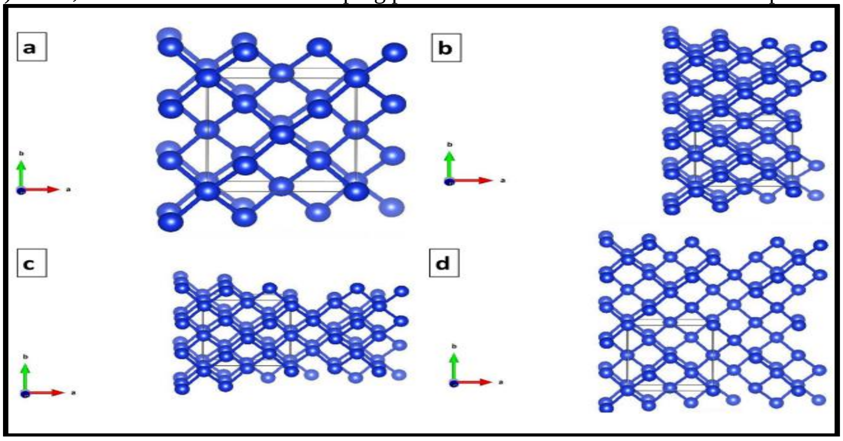

Fig.6 a) Arrangement of 2 gm NPS powder at hydrothermal time of 3 hr at 200 C^o; b) (NPS-B) doping with 0.5 gm of H_3BO_3; c) (NPS-Ni) doping with 0.5 gm $NiCl_2·6H_2O$; and d) (NPS-Cd) doping with 0.5 gm $CdCl_2·2.5H_2O$.

3.2. Energy Dispersive X- Ray (EDX) Analysis

The presence of elements Si, O, B, Ni, and Cd was confirmed by EDX analysis, which presents the percentages of doped powder components. Three elemental peaks are identified: one at 1.8 and 2.0 keV for the element silicon; one at 0.57 keV for the element oxygen, as shown in Fig. 7(a-c); one at 0.1 and 0.30 keV for the element boron, as shown in Fig. 7(a); one at 0.7 and 7.5 keV for the element nickel, as shown in Fig. 7(b); and one at 3.2 keV for the element cadmium, as shown in Fig. 7(c). Table 2 displays that NPS has been successfully doped with B, Ni, and Cd, according to the EDX data, and the atomic percentage of B 8.13% is the best doping ratio because it represents the highest incorporation of the dopant B into the NPS structure compared to the Ni- and Cd-doped samples. The higher atomic percentage of boron suggests a more effective integration into the material, which can enhance its properties. Additionally, the corresponding weight percentage (4.68%) indicates a substantial presence of boron without excessively compromising the silicon and oxygen content, ensuring structural stability.

Table 2: Results of EDX analysis

Samples	(B-Ni-Cd K)		(O K)		(Si K)	
	Weight %	Atomic %	Weight %	Atomic %	Weight %	Atomic %
NPS-B	4.68	8.13	47.08	55.23	43.32	28.95
NPS-Ni	2.19	1.66	5.06	12.15	92.74	86.19
NPS-Cd	3.48	1.31	3.25	8.81	93.25	89.88

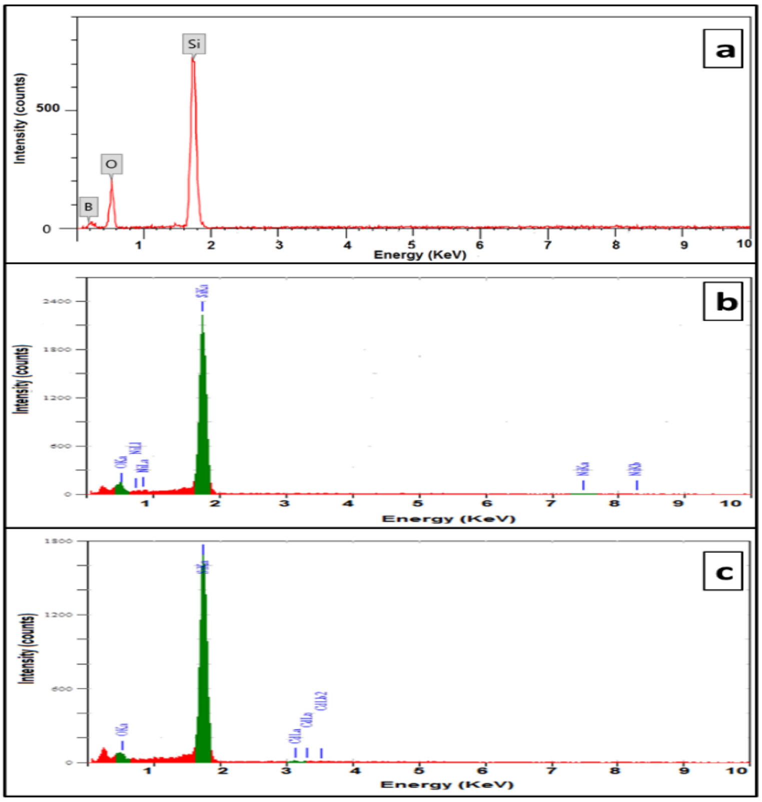

Fig.7 EDX spectra of 2 gm NPS powder at hydrothermal time of 3 hr at 200 C^o; a) (NPS-B) doping with 0.5 gm of H_3BO_3, b) (NPS-Ni) doping with 0.5 gm $NiCl_2 \cdot 6H_2O$, and c) (NPS-Cd) doping with 0.5 gm $CdCl_2 \cdot 2,5H_2O$.

3.3. Fourier Transform Infrared Spectrophotometer (FTIR) Analysis

Infrared transmittance analysis tells us about the surface chemistry of powders and how the doping material affects them. The doped NPS-B is shown in Fig. 8(a); the asymmetric stretching bond (Si–O) in (Si–O–Si) is ascribed to the band in the 1000–1300 cm^{-1} range. Additionally, the FTIR band at 481 cm^{-1} is caused by bending vibrations (O–Si–O), whereas the band at 819 cm^{-1} corresponds to symmetric stretching vibrations (Si–O–Si). The wavenumber value at which the NPS powder is created is 1120 cm^{-1}. Apart from the vibration in the water of 1673 cm^{-1} resulting from O-H scissor bending, the broad band in the 3497 cm^{-1} range is indicative of (O-H) stretching modes in H_2O and SiOH groups [34]. Finally, the bands in the region of 1350-1400 cm^{-1} are due to the stretching bond (B–O) [35]. In addition, the intensity of the NPS peak at 1100 cm^{-1} in NPS-B (1.098) is less than the original intensity in NPS (2.895). The decrease in the intensity can be attributed to the successful incorporation of B into the NPS structure. This reduction suggests that boron doping alters the (Si–O–Si) network, leading to structural modifications that affect bond vibrations and weaken or disrupt the original asymmetric stretching vibrations, causing a decrease in peak intensity. The presence of B atoms in NPS was confirmed by the EDX analysis Fig. 7(a).

The doped NPS-Ni is shown in Fig. 8(b); the FTIR band at 481 cm^{-1} is corresponds to bending vibrations (O–Si–O). A new peak with a centre at 670 cm^{-1} is observed, and it is typically linked to Ni-O bonds [36]. When NiO forms, it means that Ni is not deposited on NPS as an oxide (Si-O-Ni), but rather in its metallic form. The presence of Ni atoms in NPS was confirmed by EDX analysis Fig. 7(b). In Fig. 8(c), the cadmium bond is supposed to appear at 794 cm^{-1} as shown in the previous studies [37]. But, in case of this work, it wasn't observed. This is due to the minimal quantity of dopant (cadmium chloride) that was used and suggesting that due to possible weak bonding, structural disorder, interference from Si–O bonds, or Cd existing in a different chemical form. The primary IR peak assignments are listed in Table 3.

Table 3: Peaks in FTIR spectra of NPS after doping

Peaks (cm^{-1})	**Assignment**
1000–1300	(Si–O) and (Si–O–Si) asymmetric stretching
481	(O–Si–O) bending vibrations
819	(Si–O–Si)symmetric stretching vibrations
1120	NPS
1673	(O-H) vibration scissor bending
3497	(O-H) stretching modes and SiOH groups
1350-1400	(B–O)
670	(Ni-O)

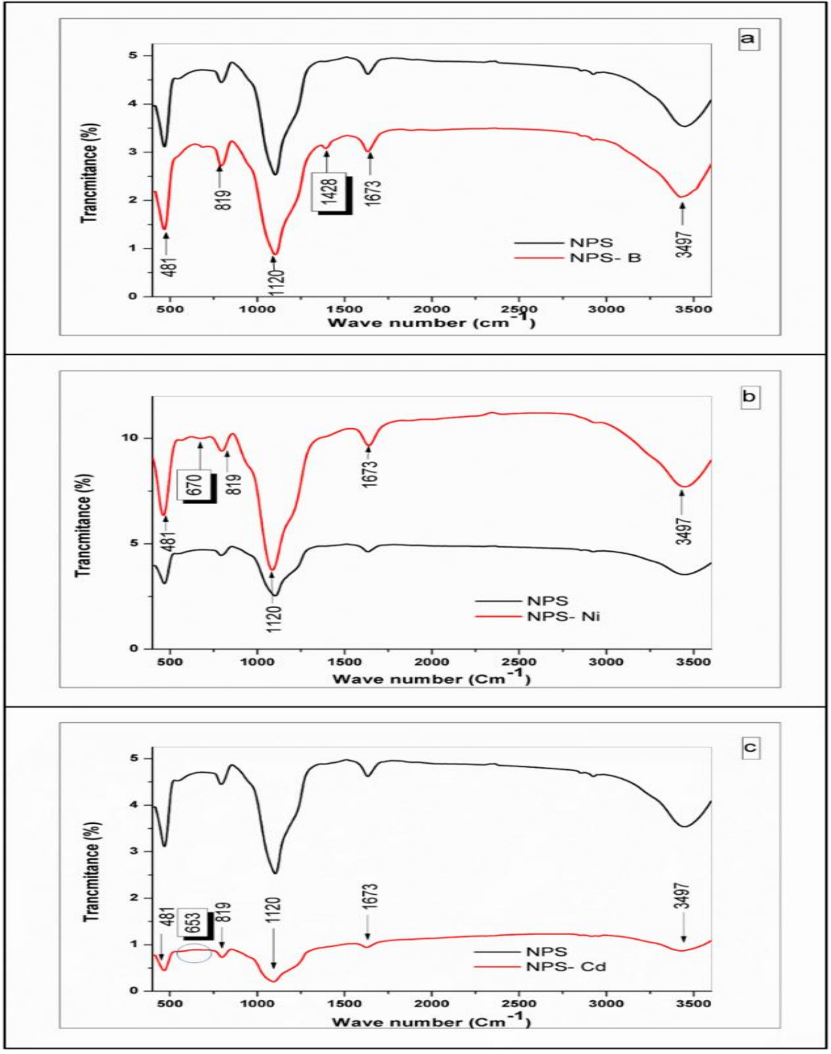

Fig.8 FTIR spectra of 2 gm NPS powder at hydrothermal tim of 3 hr at 200 C°; a) (NPS-B) doping with 0.5 gm of H_3BO_3, b) (NPS-Ni) doping with 0.5 gm $NiCl_2·6H_2O$, and c) (NPS-Cd) doping with 0.5 gm $CdCl_2·2,5H_2O$.

3.4. Scanning Electron Microscopy (SEM)

The size and morphology of the particles are revealed by SEM analysis. NPS particle size is also influenced by a few variables, such as hydrothermal time and the concentration of doping material. Fig. 9 shows SEM micrographs of the NPS doped with boron. Doped powders are made up of agglomerates of relatively small, porous particles with uneven shapes. As a result of the hydrothermal technique, NPS appeared with small particles interpreted as B molecules in NPS-B. Fig. 9(d) shows the corresponding size distribution histograms and the variation of average size with respect to dopant concentrations. The formation of nanoparticles of a spherical and rods morphology and narrow size distribution can be seen from the SEM micrographs, with an average diameter of 125 nm, suggesting that the enhancement of particle size is due to the agglomeration of NPS particles via adding dopant materials.

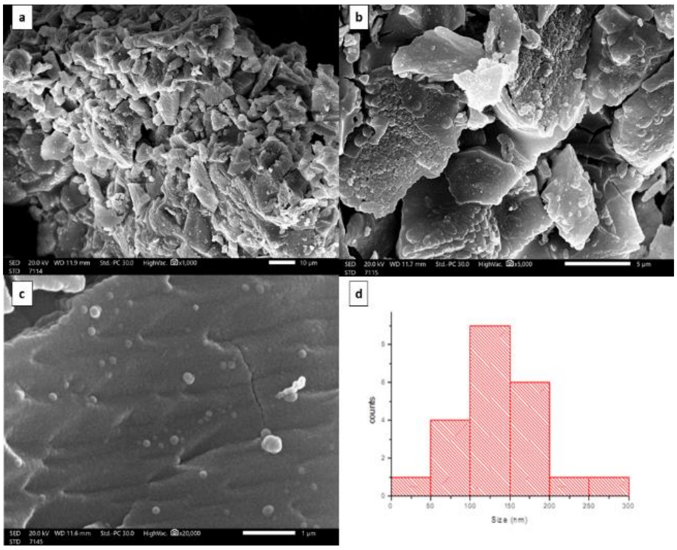

Fig.9 SEM micrograph of NPS doped with boron at various magnifications; a) 1000, b) 5000, c) 20000, and d) grain size distribution.

Fig.10 in NPS-Ni indicates that particles are in the shape of rods array, as shown in Figs. 10 (a,b) and small Ni particles are interpreted, in addition to the formation of nano-clusters due to the agglomeration process. Fig. 10(d) shows the average size of the nanoparticle observed from SEM images is 125 nm too.

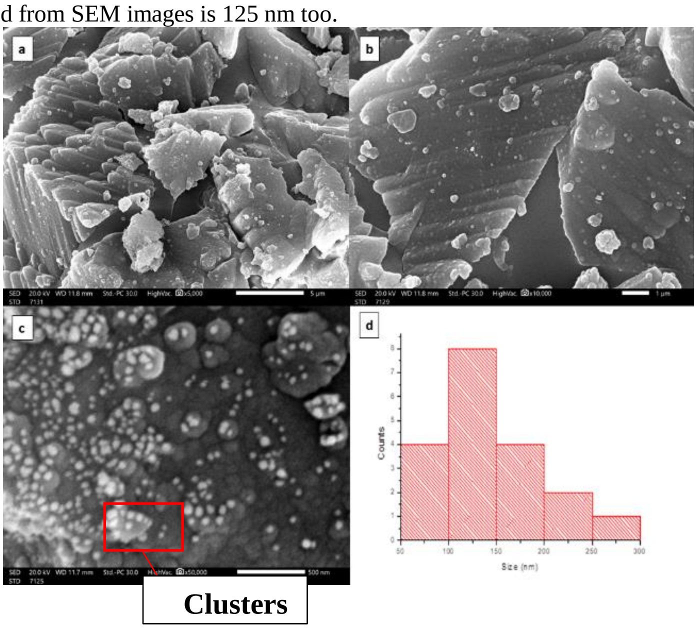

Fig.10 SEM micrograph of NPS doped with nickel at various magnifications; a) 5000, b) 10000, c) 50000, and d) grain size distribution.

Fig. 11 indicates particles of Cd that are dopants in NPS rod arrays for the formation of NPS-Cd. In addition, the small particles of Cd are interpreted into nano-clusters of NPS via the agglomeration process. Fig. 11(d) shows the average size distribution that can be seen from the SEM micrographs with an average diameter of 40 to 170 nm.

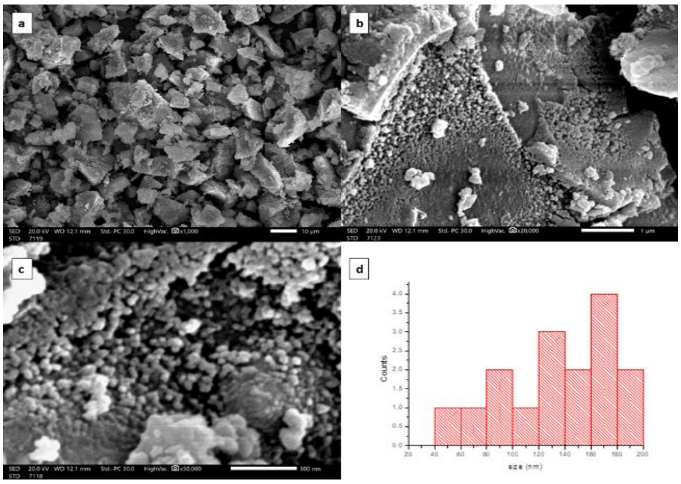

Fig.11 SEM micrograph of NPS doped with cadmium at various magnifications; a) 1000, b) 20000, c) 50000, and d) grain size distribution.

3.5. Optical properties of NPS powder with dopant materials

Using a UV-VIS double beam spectrophotometer, the optical absorption spectra of the NPS powder samples containing dopant material were captured in the 400–1000 nm region. Fig. 12 shows the variation in optical absorbance with the dopant materials to determine the band gap. A plot of $(\alpha h\upsilon)^2$ against $h\upsilon$. The energy gap E_g can be found using the Stern equation for near-edge absorption [35]:

$$\alpha = \frac{A(h\upsilon - E_g)^{\frac{n}{2}}}{h\upsilon} \quad (1)$$

Where A is constant, E_g is the band gap, α is absorbance, υ is the frequency of the radiation, h is Planck's constant and n is an important factor that detects the type of existing transition that carries a value of either 1 or 4. Given that NPS and the majority of semiconductors have indirect band gaps. By taking the linear component of the curve towards zero absorption ((αhv)2 = 0), one may get Eg [36]. The band gap of NPS powders with different doping materials was determined by drawing a graph of (αhυ)2 against hυ and then extending the straight line segment to the energy axis [37]. The band gap of various NPS powders can be found using the Tauc plot.

The optical absorption measurements (UV) carried out for NPS-B, NPS-Ni, and NPS-Cd in this work observed a decrease in optical band gap of 2.0, 1.7, and 1.6 eV compared with the optical band gap of NPS in the previous work [11]. These values decreased as the electronegativity of boron, nickel, and cadmium decreased by 2.04, 1.91, and 1.69, respectively [41]. This observation was further supported by the energy calculations of the prepared NPS samples. The electronegativity and electronic polarizability values are attributed to the increase in atomic radius of boron, nickel, and cadmium (85, 135, and 155 pm, respectively). The observed band gap decrease is a result of a combination of impurity-induced states, quantum confinement reduction, defect formation, and carrier-induced band renormalization. Each dopant influences the electronic structure differently, leading to varying degrees of band gap narrowing.

Table 4: Band gap of PS and Various Doped/Deposited Structures

Sample name	**Band gap (eV)**	**Ref**
NPS	2.4	[11]
NPS-B	2.0	This work
NPS-Ni	1.7	This work
NPS-Cd	1.6	This work
boron-doped Si wafers	2.0	[42]
Cadmium sulfide (CdS) deposited on porous by spin coating technique	2.7	[43]
CdS deposited on p-type PS	2.39 and 2.43	[44]
CdS-PS: p-Si heterostructures	2.6	[45]
ZnO-PS: p-Si heterostructures	3.3	[45]
Au:Cd deposited on PS was prepared via laser ablation	3.6 and 4.8	[46]
GaN thin film was deposited on PS	3.36 eV and 1.7 eV	[47]
AlGaN/PS	3.2 eV,3.44 eV, and 3.6 eV	[48]

The addition of dopant materials to NPS samples results in a decrease in band gap according to optical absorption studies. Table 4 illustrates that the band gap obtained for NPS-Cd is the smallest value among all published values, suggesting a significant modification of the electronic structure. In contrast, heterostructures involving CdS, ZnO, Au:Cd, GaN, and AlGaN on PS show higher band gaps, demonstrating how different materials influence the optical properties of PS.

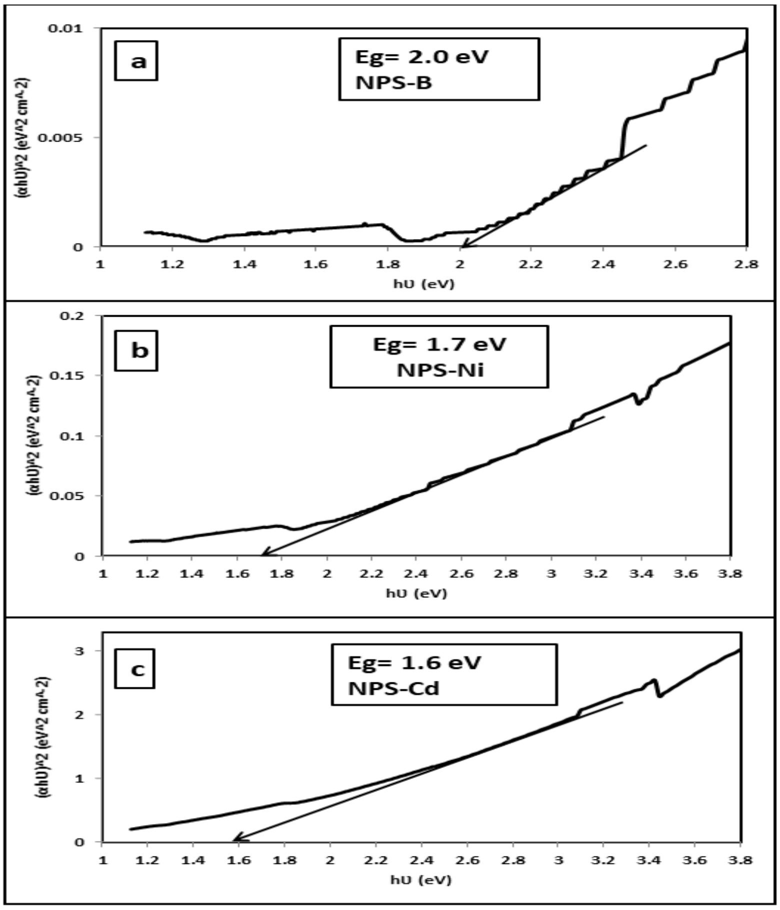

Fig.12 A graph showing photon energy (hν) vs energy square $(\alpha h\nu)^2$; a) (NPS-B) doping with 0.5 gm of H_3BO_3; b) (NPS-Ni) doping with 0.5 gm $NiCl_2\cdot6H_2O$; and c) (NPS-Cd) doping with 0.5 gm $CdCl_2\cdot2{,}5H_2O$.

Future prospects

The future viability and broad acceptance of p-NPS based sensors will be largely dependent on ongoing research and technological developments.

4. Conclusions

In this work, we successfully synthesized doped p-type NPS powder with B, Ni, and Cd using an economic and scalable hydrothermal approach. Structural characterization confirmed the incorporation of dopant atoms into the NPS framework, influencing its crystallinity and morphology. Optical studies revealed a notable decrease in the band gap of doped NPS samples compared to un-doped NPS, with NPS-Cd exhibiting the lowest band gap (1.6 eV). This reduction is primarily attributed to the introduction of impurity states, charge carrier interactions, and lattice distortions. The findings demonstrate the potential of doped NPS materials for enhanced optoelectronic applications, paving the way for their use in photo-detectors and sensors.

5. Conflicts of interest

There are no conflicts to declare.

6. Formatting of funding sources

The authors declare that no funds, grants, or other support were received during the preparation of this manuscript.

7. References

[1] H. Föll, M. Christophersen, J. Carstensen, and G. Hasse, Formation and application of porous silicon. Materials Science and Engineering: R: Reports. 39 (2002) 93-141. https://doi.org/10.1016/S0927-796X(02)00090-6

[2] V. Parkhutik, Porous silicon—mechanisms of growth and applications. Solid-State Electronics. 43 (1999) 1121-1141. https://doi.org/10.1016/S0038-1101(99)00036-2

[3] R. Moretta, L. De Stefano, M. Terracciano, and I. Rea, Porous silicon optical devices: recent advances in biosensing applications. Sensors. 21 (2021) 1336. https://doi.org/10.3390/s21041336

[4] H. A. Santos, Porous silicon for biomedical applications. (2014) 535-554. https://doi.org/10.1533/9780857097156.1.129

[5] N. H. Al-Hardan, M. A. Abdul Hamid, N. M. Ahmed, A. Jalar, R. Shamsudin, N. K. Othman, L. Kar Keng, W. Chiu, and H. N. Al-Rawi, High sensitivity pH sensor based on porous silicon (PSi) extended gate field-effect transistor. Sensors. 16 (2016) 839. https://doi.org/10.3390/s16060839

[6] G. Tuci, Y. Liu, A. Rossin, X. Guo, C. Pham, G. Giambastiani, and C. Pham-Huu, Porous silicon carbide (SiC): a chance for improving catalysts or just another active-phase carrier? Chemical Reviews. 121 (2021) 10559-10665. https://doi.org/10.1021/acs.chemrev.1c00269

[7] I. A. Levitsky, Porous silicon structures as optical gas sensors. Sensors. 15 (2015) 19968-19991. https://doi.org/10.3390/s150819968

[8] M. Nabil, K. R. Mahmoud, R. Nomier, E. M. El-Maghraby, and H. Motaweh, Nano-Porous-Silicon Powder as an Environmental Friend. Materials (Basel). 14 (2021) 4252. https://doi.org/10.3390/ma14154252

[9] K. Guo, A. Sharma, R. J. Toh, E. Alvárez de Eulate, T. R. Gengenbach, X. Cetó, N. H. Voelcker, and B. Prieto-Simón, Porous silicon nanostructures as effective faradaic electrochemical sensing platforms. Advanced Functional Materials. 29 (2019) 1809206. https://doi.org/10.1002/adfm.201809206

[10] A.-H. Kashyout, H. M. Soliman, M. Nabil, and A. A. Bishara, Fabrication of nano-porous silicon using alkali etching process. Materials Letters. 100 (2013) 184-187. https://doi.org/10.1016/j.matlet.2012.12.107

[11] M. M. Nabil, K. M. Mahmoud, R. Nomeir, E.-M. El-Maghraby, and H. Motaweh, 3D porous silicon (nanorods array, nanosheets, and nanoclusters) production. Egyptian Journal of Chemistry. 63 (2020) 1269-1278. https://doi.org/10.21608/EJCHEM.2019.14613.1885

[12] X. Pi, Doping silicon nanocrystals with boron and phosphorus. Journal of Nanomaterials. 2012 (2012) 912903. https://doi.org/10.1155/2012/912903

[13] L. Fabry, R. Hoelzl, A. Andrukhiv, K. Matsumoto, J. Qiu, S. Koveshnikov, M. Goldstein, A. Grabau, H. Horie, and R. Takeda, Test methods for measuring bulk copper and nickel in heavily doped p-type silicon wafers. Journal of the Electrochemical Society. 153 (2006) G566. https://doi.org/10.1149/1.2186799

[14] A. Istratov, P. Zhang, R. McDonald, A. Smith, M. Seacrist, J. Moreland, J. Shen, R. Wahlich, and E. Weber, Nickel solubility in intrinsic and doped silicon. Journal of Applied Physics. 97 (2005) https://doi.org/10.1063/1.1836852

[15] E. Pérez, H. Castán, H. García, S. Dueñas, L. Bailón, D. Montero, R. García-Hernansanz, E. García-Hemme, J. Olea, and G. González-Díaz, Energy levels distribution in supersaturated silicon with titanium for photovoltaic applications. Applied Physics Letters. 106 (2015) https://doi.org/10.1063/1.4905784

[16] J. Bodunrin, D. Oeba, and S. Moloi, Current-voltage and capacitance-voltage characteristics of cadmium-doped p-silicon Schottky diodes. Sensors and Actuators A: Physical. 331 (2021) 112957. https://doi.org/10.1016/j.sna.2021.112957

[17] J. Zhang, X. Zhou, J. Tang, Y. Ren, M. Jiang, Y. Tang, H. Wang, and J. Yang, Phosphoric acid induced homogeneous crosslinked phosphorus doped porous Si nanoparticles with superior lithium storage performance. Applied Surface Science. 509 (2020) 144873. https://doi.org/10.1016/j.apsusc.2019.144873

[18] L. Scheffler, V. Kolkovsky, and J. Weber, Electrical levels in nickel doped silicon. Journal of Applied Physics. 116 (2014) https://doi.org/10.1063/1.4901003

[19] M. Li, M. Hu, W. Yan, S. Ma, P. Zeng, and Y. Qin, NO2 sensing performance of p-type intermediate size porous silicon by a galvanostatic electrochemical etching method. Electrochimica Acta. 113 (2013) 354-360. https://doi.org/10.1016/j.electacta.2013.09.120

[20] J. L. Gole, and S. E. Lewis, Porous Silicon – Sensors and Future Applications. (2008) 149-175. https://doi.org/10.1016/b978-008044528-1.50005-1

[21] W. Liu, Y. Yun, M. Li, J. Mao, C. Li, C. Li, and L. Hu, Preparation of hollow ceramic photocatalytic membrane grafted with silicon-doped TiO2 nanorods and conversion of high-concentration NO. Chemical Engineering Journal. 437 (2022) 135261. https://doi.org/10.1016/j.cej.2022.135261

[22] T. Paul, J. J. Palakulam, N. Unnikrishnan, R. Philip, and K. A. Mary, Warm to cool tunable ultra-stable white light emissions from carbon dots-Tb3+-Eu3+ doped silica. Optical Materials. 138 (2023) 113673. https://doi.org/10.1016/j.optmat.2023.113673

[23] K. Byrappa, and T. Adschiri, Hydrothermal technology for nanotechnology. Progress in crystal growth and characterization of materials. 53 (2007) 117-166. https://doi.org/10.1016/j.pcrysgrow.2007.04.001

[24] Y. Mao, T. J. Park, F. Zhang, H. Zhou, and S. S. Wong, Environmentally friendly methodologies of nanostructure synthesis. Small. 3 (2007) 1122-1139. https://doi.org/10.1002/smll.200700048

[25] Available from: https://www.webelements.com/atom_sizes.html.

[26] A. Altomare, F. Capitelli, N. Corriero, C. Cuocci, A. Falcicchio, A. Moliterni, and R. Rizzi, The Rietveld refinement in the EXPO software: A powerful tool at the end of the elaborate crystal structure solution pathway. Crystals. 8 (2018) 203. https://doi.org/10.3390/cryst8050203

[27] T. Runcevski, and C. M. Brown, ACS Publications, Cryst. Growth Des. (2021). https://doi.org/10.1021/acs.cgd.1c00854

[28] J. S. Evans, and I. R. Evans, Structure analysis from powder diffraction data: Rietveld refinement in excel. Journal of Chemical Education. 98 (2020) 495-505. https://doi.org/10.1021/acs.jchemed.0c01016

[29] M. Wang, Y. Lu, J. Lan, T. Wang, C. Zhang, Z. Cao, T. Li, and P. K. Liaw, Lightweight, ultrastrong and high thermal-stable eutectic high-entropy alloys for elevated-temperature applications. Acta Materialia. 248 (2023) 118806. https://doi.org/10.1016/j.actamat.2023.118806

[30] Available from: https://environmentalchemistry.com/yogi/periodic/ionicradius.html.

[31] K. Rumpf, P. Granitzer, G. Hilscher, M. Albu, and P. Poelt, Magnetically interacting low dimensional Ni-nanostructures within porous silicon. Microelectronic engineering. 90 (2012) 83-87. https://doi.org/10.1016/j.mee.2011.05.016

[32] M. A. Alam, S. Ahmed, R. K. Bishwas, S. Mostofa, and S. A. Jahan, X-ray crystallographic diffraction study by whole powder pattern fitting (WPPF) method: Refinement of crystalline nanostructure polymorphs TiO2. South African Journal of Chemical Engineering. 51 (2025) 68-77. https://doi.org/10.1016/j.sajce.2024.10.010

[33] F. Izumi, and K. Momma, Three-dimensional visualization in powder diffraction. Solid State Phenomena. 130 (2007) 15-20. https://doi.org/10.4028/www.scientific.net/SSP.130.15

[34] M. Nabil, and H. A. Motaweh, Enhanced thermal stability of promising nano-porous silicon powder. Advances in Nanoparticles. 05 (2016) 199-205. https://doi.org/10.4236/anp.2016.54021

[35] M. Khalifa, M. Atyaoui, M. Hajji, R. Ouertani, and H. Ezzaouia, Purification of metallurgical-grade silicon powder via chemical attack by hydrofluoric and nitric acids followed by thermal treatment. Materials Science in Semiconductor Processing. 16 (2013) 1742-1746. https://doi.org/10.1016/j.mssp.2013.06.006

[36] A. Kalam, A. S. Al-Shihri, A. G. Al-Sehemi, N. Awwad, G. Du, and T. Ahmad, Effect of pH on solvothermal synthesis of β-Ni (OH) 2 and NiO nano-architectures: surface area studies, optical properties and adsorption studies. Superlattices and Microstructures. 55 (2013) 83-97. https://doi.org/10.1016/j.spmi.2012.11.024

[37] M. M. Al-Mogren, and A.-N. M. Alaghaz, Synthesis, Spectral and Quantum Chemical Calculations of Mononuclear Nickel (II), Copper (II) and Cadmium (II) Complexes of New Schiff–Base Ligand. International Journal of Electrochemical Science. 8 (2013) 8669-8685. https://doi.org/10.1016/S1452-3981(23)12918-X

[38] M. Nabil, F. Horia, S. Fouad, and S. Negm, Impact of Au nanoparticles on the thermophysicalparameters of Fe3O4 nanoparticles for seawater desalination. Optical Materials. 128 (2022) 112456. https://doi.org/10.1016/j.optmat.2022.112456

[39] W. Aperador, L. Yate, M. Pinzón, and J. Caicedo, Optical and semiconductive properties of binary and ternary thin films from the Nb-Ti-O system. Results in Physics. 9 (2018) 328-336. https://doi.org/10.1016/j.rinp.2018.02.060

[40] B. C. Dev, M. H. Babu, J. Podder, S. Sagadevan, and A. Zubair, Low temperature synthesis of α-and β-phase Bi 2 O 3 thin film via B doping: tailoring optical band gap and n-to p-type Bi 2 O 3. Journal of Materials Science: Materials in Electronics. 30 (2019) 15670-15682. https://doi.org/10.1007/s10854-019-01950-5

[41] Available from: https://en.wikipedia.org/wiki/Electronegativities_of_the_elements_(data_page).

[42] L. Burstein, Y. Shapira, J. Partee, J. Shinar, Y. Lubianiker, and I. Balberg, Surface photovoltage spectroscopy of porous silicon. Physical Review B. 55 (1997) R1930-R1933. https://doi.org/10.1103/PhysRevB.55.R1930

[43] M. W. Eesa, Porous Silicon effect on the performance of CdS nanoparticles photodetector. Iraqi Journal of Physics. 14 (2016) 129-137. https://doi.org/10.30723/ijp.v14i31.180

[44] R. A. Ismail, A.-M. E. Al-Samarai, and A. Y. Ali, Preparation and characteristics study of CdS/macroporous silicon/c-Si double heterojunction photodetector by spray pyrolysis technique. Optik. 168 (2018) 302-312. https://doi.org/10.1016/j.ijleo.2018.04.101

[45] M. Das, S. Sarmah, and D. Sarkar, Photo sensing property of nanostructured CdS-porous silicon (PS):p-Si based MSM hetero-structure. Journal of Materials Science: Materials in Electronics. 30 (2019) 11239-11249. https://doi.org/10.1007/s10854-019-01470-2

[46] E. M. Sulaiman, U. M. Nayef, and F. A. H. Mutlak, Synthesis of Au-Cd ablated on porous silicon for photodetector applications. Materials Technology. 37 (2022) 2711-2717. https://doi.org/10.1080/10667857.2022.2059202

[47] M. A. Fakhri, H. D. Jabbar, M. J. AbdulRazzaq, E. T. Salim, A. S. Azzahrani, R. K. Ibrahim, and R. A. Ismail, Preparation of GaN/Porous silicon heterojunction photodetector by laser deposition technique. Scientific Reports. 13 (2023) 14746. https://doi.org/10.1038/s41598-023-41396-8

[48] A. R. Abbas, M. A. Fakhri, A. A. Alwahib, E. T. Salim, A. B. Ali, A. S. Azzahrani, and S. C. Gopinath, Synthesized aluminum gallium nitride/porous-Si thin films at different compositions by pulsed laser deposition method. Physica Scripta. 100 (2024) 015502. https://doi.org/10.1088/1402-4896/ad92c5